# Influence of the background state on Rossby wave propagation into the Great Lakes region based on observations and model simulations

Kathleen D. Holman[1,2] * David J. Lorenz[1]

Michael Notaro[1]

*1. Nelson Institute Center for Climatic Research, University of Wisconsin-Madison, Madison, WI, USA.*

*2. Department of Atmospheric and Oceanic Sciences, University of Wisconsin-Madison, Madison, WI, USA.*

* *Corresponding author address:* Kathleen D. Holman, Department of Atmospheric and Oceanic Sciences, University of Wisconsin-Madison 1225 W. Dayton St., Madison, WI 53706.
E-mail: kathleendeeholman@gmail.com

## ABSTRACT

We investigate the relationship between hydrology in the Great Lakes basin, namely over-lake precipitation, and transient Rossby waves using the National Centers for Environmental Predictions-National Center for Atmospheric Research (NCEP-NCAR) Reanalysis data and historical output from the third phase of the Coupled Model Intercomparison Project (CMIP3). The preferred path of observed Rossby wave trains associated with over-lake precipitation on Lake Superior depends strongly on season and appears related to the time-mean, upper-level flow. During summer and fall, the Northern Hemisphere extratropical jet is relatively narrow and acts as a waveguide, such that Rossby wave trains traversing the Great Lakes region travel along the extratropical Pacific and Atlantic jets. During other months, the Pacific jet is relatively broad, which allows more wave activity originating in the tropics to penetrate into the mid-latitudes and influence Lake Superior precipitation. Analysis is extended to CMIP3 models and is intended to 1) further our understanding of how variations in the mean state influence transient Rossby waves and 2) assess models' ability to capture observed features, such as wave origin and track. Results indicate that Rossby wave train propagation in 20th century simulations can significantly differ by model. Unlike observations, some models do not produce a well-defined jet across the Pacific Ocean during summer and autumn. In these models, some Rossby waves affecting the Great Lakes region originate in the tropics. Collectively, observations and model results show the importance of the time-mean, upper-level flow on Rossby wave propagation and therefore, on the relative influence of the tropics versus the extratropics on the hydroclimate of the Great Lake region.

# 1. Introduction

The intersection of regional hydrology and large-scale atmospheric circulation patterns remains an active and continuously evolving area of research. Many of the previous studies involving Midwest and Great Lakes hydrology focus on the relationship with pre-defined teleconnection patterns and associated time series, such as the Pacific-North American (PNA) teleconnection pattern (Rodionov 1994; Grover and Sousounis 2002; Coleman and Rogers 2003; Ghanbari and Bravo 2008), the Atlantic Multidecadal Oscillation (Hanrahan et al. 2010), and the El Niño-Southern Oscillation (Rodionov and Assel 2000; Assel et al. 2000; Rogers and Coleman 2003). Rather than exploring the direct link between atmospheric circulations and hydrology, those studies utilize simplified indices of the atmospheric circulation. Outside of the Great Lakes community however, there has been a recent interest in connecting regional hydrology directly to atmospheric circulations, namely through transient Rossby waves. For example, results from Ding and Wang (2005) indicate that summer precipitation over East Asia, the North Pacific, and parts of North America is related to a zonally-elongated Rossby wave packet, referred to as the circumglobal teleconnection pattern (CGT; Branstator 2002). Feldstein and Dayan (2008) identify a relationship between winter precipitation over Israel and an eastward-propagating Rossby wave that originates over the northeast Pacific. Results from Martius et al. (2008) indicate that heavy precipitation events along the Alpine south-side are preceded by Rossby wave trains throughout the year. Similarly, Wang et al. (2010) suggest that anomalously wet conditions over Utah during June 2009 were the result of a short Rossby wave train propagating along the extratropical jet stream. These studies, along with others, demonstrate that Rossby waves modulate regional climate, including precipitation, yet the relationship with hydrology in the Great Lakes region has yet to be investigated.

Rossby waves owe their existence to gradients in the potential vorticity (PV) field. Since the jet stream is associated with strong gradients in PV, Rossby waves are modified by the basic state (i.e. background flow) within which they are embedded (Hoskins and Karoly

1981; Hoskins and Ambrizzi 1993; Kosaka et al. 2009). Researchers have developed a variety of modeling experiments and observational diagnostics to understand how changes in the basic-state influence Rossby wave propagation, including barotropic models (Hoskins and Karoly 1981; Branstator 1983), baroclinic models (Held 1983; Lee and Held 1993; Yun et al. 2011), general circulation models (GCMs; Barnes and Hartmann 2011), and reanalysis data (Branstator 2002; Martius et al. 2010). Some historical modeling studies employ homogeneous or zonally-symmetric wind profiles (Hoskins et al. 1977; Opsteegh and Van den Dool 1980; Hoskins and Karoly 1981), while other approaches increase complexity by accounting for longitudinal variations in the basic-state (Branstator 1983; Karoly 1983; Hoskins and Ambrizzi 1993). Overall, results indicate that Rossby wave propagation is strongly influenced by both zonal and meridional variations in the upper-level wind field. In the absence of strong gradients in the mean background state, Rossby waves follow a great-circle path, while Rossby waves propagating within a strong jet tend to be refracted back toward the jet core resulting in zonally-oriented chains of anomalies along the axis of the jet. In other words, upper-level jet streams act as waveguides, focusing and trapping perturbations, resulting in relationships or teleconnections between widely separated regions of the globe (Branstator 2002; Martius et al. 2010).

Newman and Sardeshmukh (1998) investigate the monthly evolution of the observed Rossby waveguide, which they define by a gradient in the absolute vorticity field on an upper-level, isobaric surface. Their results indicate that the structure of the Rossby waveguide over the Pacific Ocean changes throughout the year, influencing the forcing region important for disturbances traversing the United States. For example, the United States is sensitive to forcing over the eastern Pacific during winter months, while the western Pacific becomes more important during the late spring. Based on their analysis of the absolute vorticity field, the winter Rossby waveguide is centered near 30°N and extends into the eastern Pacific, where there exists a westerly duct that allows for tropical-extratropical interactions and cross-equatorial flows (Webster and Holton 1982; Knippertz 2005). Alternatively, the average summer waveguide is straddled by a negative absolute vorticity gradient to the north and south, blocking the westerly wind duct and steering Rossby waves across the Pacific toward the east coast of North America. These differences in the structure of the Rossby waveguide over the Pacific Ocean likely influence climatic conditions downstream.

Later studies agree with results from Newman and Sardeshmukh (1998), suggesting that the structure and location of the Rossby waveguide change with the basic state (Ding and Wang 2005; Martius et al. 2008; Yun et al. 2011). Ding and Wang (2005), for instance, consider differences in Rossby wave train paths across the Pacific Ocean during summer months (June-September). According to their analysis, Rossby wave trains follow the westerly jet in each month and migrate northward with the seasonal cycle of the jet stream. In addition, the waveguide is weaker and the wavelength of Rossby waves is shorter in July, compared to June. Yun et al. (2011) analyze the impact of the basic state on Rossby wave propagation in a linearized barotropic model during July and August. Their results suggest that the extratropical response to diabatic forcing in the mid-latitudes is typically larger under August conditions than July conditions, due to changes in the mean vorticity and divergence fields between the two months. Their results emphasize the importance of monthly, rather than seasonal, analyses in exploring and understanding Rossby wave propagation.

In this paper, we expand on previous research by exploring the direct relationship between precipitation in the Great Lakes region and large-scale atmospheric circulation patterns, namely atmospheric Rossby waves. Using reanalysis data, we explore how variability in the upper-level wind field on a monthly timescale influences the origin and path of the Rossby waves that traverse the Great Lakes basin. To further demonstrate how variations in the basic-state influence Rossby waves that traverse the Great Lakes region, we examine transient Rossby waves simulated by 16 different GCMs that participated in the third phase of the Coupled Model Intercomparison Project (CMIP3). The analysis of simulated Rossby waves is motivated by the fact that reanalysis data provide a limited sample of atmospheric background states, and using multiple GCMs with different basic-states may aid in illuminating the effects of variations in the mean-state more easily. In addition, the analysis of simulated Rossby waves serves two primary purposes. The first is to use these models to improve our understanding of underlying relationships between Rossby waves and the upper-level mean flow, while the second is to explore models' reliability in representing these drivers of regional hydrology. In light of future climate projections that suggest a strengthening and poleward shift of the extratropical jet stream (Kushner et al. 2001; Lorenz and DeWeaver 2007), results from this study may provide useful for future climate model development and assessing model uncertainty with implications for future water resources in the Great Lakes region.

The remainder of the paper is structured as follows. Section 2 includes a description of the observational datasets and model ouput. Analysis of observed Rossby waves that are associated with over-lake precipitation in the Great Lakes region is presented in section 3. Model-simulated Rossby waves are analyzed in section 4. Finally, section 5 contains a summary of our results.

## 2. Data

The relationship between large-scale atmospheric circulation patterns and regional hydrology in the Great Lakes basin is established using daily over-lake precipitation estimates from the Lake Superior basin between 1948-2010. Although direct observations of over-lake precipitation are not available, the National Oceanic and Atmospheric Administration's (NOAA) Great Lakes Environmental Research Laboratory (GLERL) estimates over-lake precipitation by applying a Thiessen polygon algorithm (Croley and Hartmann 1985) to over-land precipitation observations. Records are publicly available through an online hydrological database (Croley and Hunter 1994). Some seasonal biases in over-lake precipitation are expected because the algorithm used to generate the estimates is based solely on land-based observations and does not incorporate variations in atmospheric stability over the lake surface, which is related to differences in temperature between the lake surface and overlying air (Holman et al. 2012). Because we analyze daily precipitation anomalies and perform correlation analyses on each month separately, these systematic seasonal biases should be significantly less important. Following Chatterjee and Goswami (2004) and Fujinami and Yasunari (2009), anomalies were constructed by removing the first three harmonics of the annual cycle. Rather than over-lake precipitation estimates, the analysis could have applied over-land precipitation measurements from the Lake Superior watershed. However, the two time series of daily anomalies are highly correlated (r = 0.9996), such that the results would likely be very similar.

Analyses of 300 hPa zonal ($u$) and meridional wind ($v$) observations are based on daily-averaged data, on a 2.5° latitude × 2.5° longitude grid, from the National Centers for Environmental Prediction-National Center for Atmospheric Research (NCEP-NCAR) Reanalysis (Kalnay et al. 1996) between 1948-2010. In addition to reanalysis data, daily precipitation and daily average 300 hPa $u$ and $v$ wind from 16 different coupled ocean-atmosphere GCMs (Table 1) are analyzed between 1961-2000. GCM data are part of the 20th century experiment (20C3M) from the World Climate Research Programme's (WCRP; Meehl et al. 2007) Coupled Model Intercomparison Project Phase 3 (CMIP3). Climate simulations apply both dynamical atmosphere and ocean components. Because the horizontal resolution of model output varies from 1.125° latitude × 1.125° longitude to 4° latitude × 5° longitude, all wind data are linearly interpolated to the same horizontal resolution as the NCEP-NCAR Reanalysis data. Leap days are removed from all datasets. As with the historical precipitation data, simulated precipitation and meridional wind anomalies are constructed as deviations of the daily mean from the first three harmonics of the annual cycle. This is done in observations and model simulations to isolate transient disturbances in the meridional wind field. The annual mean and seasonal cycle are not removed from upper-level zonal wind fields because the primary objective of this study is to demonstrate how variations in the *mean* background flow influence observed and simulated transient Rossby waves.

Within the subset of GCMs used in this analysis, the land surface within five models is restricted entirely to vegetation and soil types, two models have inland lake classifications, and the remaining six models include water surfaces (PCMDI 2007). The land surface types are important for this analysis because small-scale precipitation events such as lake-effect, are unlikely to be well represented.

# 3. Observed Rossby waves

## *a. Precipitation and 300 hPa meridional wind*

Analysis of Lake Superior's hydrologic budget suggests that over-lake precipitation is the largest source of water to the lake on an annual basis (Lenters 2004). The seasonal cycle of over-lake precipitation estimates (Fig. 1) is characterized by a warm season peak (May-September) typical of the Midwest, United States (Holman and Vavrus 2012), with the largest (smallest) average amount observed during September (February). The monthly standard deviation (Fig. 1) follows a similar seasonal cycle as the mean precipitation, with a minimum in February and maxima during September and June. Though studies identify a relationship between winter precipitation in the Great Lakes basin and large-scale teleconnection patterns, such as the PNA pattern (Rodionov 1994; Isard et al. 2000; Coleman and Rogers 2003; Notaro et al. 2006), the average contribution of winter (DJF) precipitation to the annual total is less than 20% in the Lake Superior basin. It is, therefore, important to investigate these relationships in all seasons, rather than only winter.

We investigate the relationship between over-lake precipitation in the Lake Superior basin and transient Rossby waves through a series of time-lag correlation maps in which the daily over-lake precipitation anomaly time series is correlated with daily observed 300 hPa meridional wind anomalies at each grid point. Specific months are presented here which demonstrate key differences in Rossby wave origin and path throughout the year, namely April, July, and December (Fig. 2). April, July, and December months are selected because they show a variety of path structures that exist throughout the year, and their results are representative of adjacent months (i.e. April is similar to March and May).

On average, during the month of April (Fig. 2a), the Pacific jet core is characterized by zonal winds between 35-40 m $s^{-1}$ across the North Pacific. Recall that the barotropic PV field associated with the background flow is related to $-\partial^2 U/\partial y^2$, such that a narrow jet, like the climatological April Pacific jet, represents a relatively strong PV gradient and waveguide. The subtropical Pacific jet located off the west coast of Mexico is longitudinally elongated and extends from the International Date Line to the Southwest United States. The eddy-driven Atlantic jet, with core speeds between 25-30 m $s^{-1}$, is oriented in a southwest-northeast direction. The subtropical Atlantic jet is characterized by a relatively zonal orientation, with zonal wind speeds that are slightly weaker than the eddy-driven, mid-latitude jet. Rossby waves (Fig. 2a) correlated with over-lake precipitation during April originate over the western Pacific and propagate along a single, relatively constant latitude band from day -4 to day -2. Day 0 correlations between over-lake precipitation and 300 hPa meridional wind peak over the Great Lakes basin and central North America. Beginning on day 0, the Rossby wave ray paths on the leading edge of the wave train diverge meridionally. By day +2, the existence of two possible tracks is suggested by local correlation maxima, although the maxima are not completely disconnected from one another.

The day 0 correlation map for April (Fig. 2a) indicates that positive over-lake precipitation anomalies are associated with southerly winds directly overhead, with northerly winds located to the west and east of the upper-level southerly flow. Alternative months show similar results for day 0 correlation maps (Fig. 2b,c). This upper-level meridional wind pattern suggests the presence of a trough-ridge couplet located over central North America, with the Great Lakes located downstream of the trough axis. Upper-level divergence associated with the eastward-moving upper-level trough supports upward vertical motion near the central US/Great Lakes region. Instantaneous correlation maps between over-lake precipitation and sea-level pressure (SLP; not shown) indicate that over-lake precipitation is associated with negative SLP anomalies to the southwest of Lake Superior, with positive SLP anomalies to the southeast throughout the year. The induced pressure gradient under such conditions is conducive for transporting warm, moist air from the Gulf of Mexico into the Great Lakes region.

During July, the zonal wind structure and preferred Rossby wave path (Fig. 2b) show different results. The climatological July extratropical jets are relatively weak and essentially zonal across the entire domain, located between 35°-50°N. Regional zonal wind speed maxima exist over the central North Pacific and near the US-Canada border, extending into the western North Atlantic, representing the cores of the extratropical jets. The subtropical branches in the North Pacific and North Atlantic are, however, essentially absent. Rossby waves associated with over-lake precipitation in July originate over the western North Pacific and propagate along a single path within the extratropical Pacific jet between day -4 and day 0. As with other months, the correlation coefficients are maximized on day 0 over central North America, including the Great Lakes basin. However, Rossby waves in July, as with the other summer months (June and August, not shown), remain trapped in the extratropical Atlantic jet beyond day 0, without propagation into the subtropics. The existence of a narrow jet over the North Pacific and North Atlantic helps to trap and focus perturbations in the midlatitude waveguide, as suggested by Branstator (2002) and Schwierz et al. (2004).

During December (Fig. 2c), the climatological Pacific jet is stronger than the April and July mean state, with average zonal speeds up to 60 m $s^{-1}$. A subtropical jet is located off the west coast of Mexico, with average zonal speeds that are much weaker than the central North Pacific jet. The eddy-driven Atlantic jet is also relatively strong during December, reaching speeds close to 40 m $s^{-1}$. The mean Atlantic jet is located over the east coast of the United States and is characterized by a slight southwest-northeast orientation. On average, Rossby waves that traverse the Great Lakes region during December (Fig. 2c) appear to originate over two different locations (day -4): the poleward flank of the Pacific jet near 60°N, which could represent a relatively weak polar jet, and the equatorward flank of the

Pacific jet, in the western central subtropical Pacific near 25°N. The two paths converge over the Gulf of Alaska and develop a meridional wind anomaly downstream over central North America (day -4 to day 0). By day 0, correlation coefficients between over-lake precipitation and meridional wind are maximized over the Great Lakes region and central North America. Beyond day 0, two propagation paths appear, including a northeastward track trapped in the Atlantic jet and a possible subtropical path that tracks towards North Africa.

The strongest correlations between over-lake precipitation anomalies and 300 hPa meridional wind anomalies occur on day 0 for each month (Fig. 3). Observed correlation values in Fig. 3 are based on locating the maximum correlation value anywhere within the domain shown in Fig. 2, regardless of location[1]. There exists a noticeable seasonal cycle in the relationship between precipitation and upper-level meridional wind, where the strongest correlations are observed during the transition seasons, such as April and October, and the weakest correlations are observed during winter months. Winter months may be characterized by the weakest correlations due to the frequent occurrence of smaller-scale precipitation events, such as lake-effect snow (Norton and Bolsenga 1993; Notaro et al. 2013). Transition seasons may be characterized by the largest correlations due to the frequent occurrence of synoptic-scale forcing, rather than convective events which occur most often during the summer months.

### *b. 300 hPa Meridional wind*

Observed Rossby waves that traverse the Great Lakes basin are further analyzed using a series of time-lag correlation maps in which the time series of daily 300 hPa meridional wind anomalies at a single point is correlated with meridional wind anomalies at every grid point (Fig. 4), an approach used by others to identify and explore Rossby waves (Chang 1993; Branstator 2002; Hakim 2003). This analysis is done to explore all Rossby waves that

[1] We identified the largest correlation value rather than picking a specific grid cell and identifying the largest correlation value at that point. Identified locations varied between 50-52.5°N and 267.5-270°E.

traverse the Great Lakes region, rather than isolating only those waves associated with over-lake precipitation. We chose a base point of 50.0°N, 267.5°E (southwest Ontario, Canada) in the 300 hPa meridional wind field because this location is characterized by the largest instantaneous (i.e. day 0) positive correlation between over-lake precipitation and 300 hPa meridional wind throughout the year (or it is located adjacent to the point with the maximum value), and would likely have the strongest relationship with water resources in the Great Lakes basin. The correlation coefficients of the wave trains displayed in Fig. 4a are larger than those identified using over-lake precipitation anomalies (Fig. 2) because the waves are identified by correlating two meridional wind time series.

Since the Rossby waves identified using the aforementioned meridional wind base point are all very similar in phase to those presented in Fig. 2 (although with greater amplitude), we present a single month, April, to avoid redundancy. On average, April Rossby wave trains that traverse the Great Lakes region originate over eastern Asia (Fig. 4a) and propagate along a single track across the North Pacific from day -4 to day -2, similar to the transient Rossby waves that influence over-lake precipitation during this month. Beyond day -2, the leading nodes spread meridionally, ultimately leading to the existence of two possible tracks by day +2. As with the other time-lag correlation plots presented here, the maximum correlation value (r=1) is achieved on day 0.

Hovmöller diagrams, which have been employed in many studies of transient atmospheric waves (Hovmöller 1949; Matthews 2000), are presented to highlight differences among observed Rossby waves that traverse the Great Lakes basin during different times of the year (Fig. 5). For an example of composite Hovmöller diagrams, see Martius et al. (2008). Here, the Hovmöller diagrams are calculated by correlating 300 hPa meridional wind anomalies at the base point (50.0°N, 267.5°E) with 300 hPa meridional wind anomalies averaged over 35°-55°N. This latitude band is selected to emphasize transient Rossby waves propagating within the extratropics. Based on the Hovmöller diagram, April Rossby waves (Fig. 5a) develop between 120°E-150°E, approximately five days prior to traversing the Great Lakes region. Wave packets retain structure in the defined latitude band for about nine days, ceasing beyond 330°E. On average, July Rossby wave trains (Fig. 5b) develop near 180°W, three to four days prior to traversing the Upper Midwest, and retain a coherent structure for approximately eight days. The December wave packet (Fig. 5c) shows minimal structure west of 180°E, and lasts for approximately one week, although the negative and positive anomaly couplet located near 230°E persists for nearly two weeks. This persistent feature likely represents the high temporal autocorrelation in the meridional wind field over the Aleutian islands (Croci-Maspoli et al. 2007) and western United States.

# 4. Simulated Rossby waves

## *a. Precipitation and 300 hPa Meridional Wind*

We analyze 20th century climate model output from 16 different GCMs (Table 1) that participated in the IPCC Fourth Assessment Report (Meehl et al. 2007) to further demonstrate how variations in the upper-level zonal wind structure influence the path of transient Rossby waves that traverse the Great Lakes region. We analyze these simulations for two main purposes. The first purpose is to qualitatively assess models' abilities to reproduce the observed origin and path of Rossby waves that are associated with precipitation and traverse the Great Lakes region, and the second is to use these models as a tool to illustrate how variations in the background state, specifically the average 300 hPa zonal-wind structure, may impact transient Rossby waves. The relationship between simulated precipitation and Rossby waves is explored using a time series of daily precipitation computed from three grid cells, including the cell closest to Lake Superior (48°N, 272°E) and the two adjacent cells directly to the west and east (totaling three grid cells), for each model and month separately. Precipitation from these grid cells is selected to represent regional precipitation in a similar manner to observations.

The seasonal cycle of average daily precipitation in the Great Lakes region from each model is shown in Figure 6, along with the multi-model average. On average, models produce a peak in average daily precipitation during late-spring to early summer (May, June, and July), with minimum values during the winter months (December, January, and February), in agreement with observations. Model spread is largest during August, June, and July, with the least amount of spread during October and May. Relative to observed estimates from GLERL, the models tend to over-produce precipitation between February and May and under-produce precipitation during the remainder of the year (Fig. 6).

As with observations, the simulated relationship between Great Lakes precipitation and atmospheric Rossby waves is explored using time-lag correlation maps between 300 hPa meridional wind anomalies at each grid cell and a base point of daily precipitation anomalies averaged over three grid cells, for each month and model separately. Rather than showing each model and month separately, multi-model average results for two contrasting months, July and December, are presented to demonstrate similarities and differences with observations, as well as to demonstrate how the simulated relationship varies throughout the year (Fig. 7).

During July (Fig. 7a), the multi-model average extratropical jets are relatively zonal across the domain. The Pacific jet extends from eastern Asia across the North Pacific towards the west coast of North America, with maximum zonal wind speeds between 15-20 m $s^{-1}$. The Atlantic jet, which is also relatively zonal across the region, reaches maximum zonal wind speeds between 20-25 m $s^{-1}$ near 45°N. Between 1961-2000, the multi-model average July zonal wind speeds are weaker than the reanalysis data south of the Aleutian Islands, near 50°N, by about 4 m $s^{-1}$. This difference, found near the observed Pacific jet maximum, could exist due to averaging over multiple models. Multi-model average zonal wind speeds are greater than the reanalysis data along the southern coast of Alaska, near 60°N, and between the equator and 35°N.

On average, simulated Rossby waves associated with precipitation over Lake Superior in July originate near the Aleutian Low around day -4 (Fig. 7a) and propagate eastward along the extratropical jet. On day 0, correlations between precipitation and upper-level meridional wind are maximized, similar to observations. Beyond day 0, nodes on the leading edge of the Rossby wave continue to propagate within the extratropical Atlantic jet, also similar to observations.

The instantaneous multi-model average spatial correlation pattern between precipitation and upper-level meridional winds strongly resembles the pattern found in observations, indicating that simulated precipitation anomalies are positively correlated with southerly wind anomalies aloft, straddled by northerly wind anomalies to the east and west. This pattern suggests that the models are able to reproduce some of the key large-scale features related to summer precipitation in the Great Lakes region.

During December (Fig. 7b), multi-model average 300 hPa zonal wind speeds are much greater than during July. The Pacific jet is characterized by wind speeds greater than 55-60 m $s^{-1}$ near the core, and wind speeds greater than 25 m $s^{-1}$ across the eastern half of the extratropical Pacific Ocean. The multi-model average Atlantic jet is oriented from southwest to northeast, similar to reanalysis data. Maximum wind speeds in the Atlantic jet are between 25-30 m $s^{-1}$. Maximum zonal wind speeds in the multi-model average Pacific jet are close to reanalysis data, while maximum zonal wind speeds in the multi-model average Atlantic jet are slightly less ($\sim$ 5 m $s^{-1}$).

Average December Rossby waves associated with precipitation in the Great Lakes region appear to originate over eastern Asia (Fig. 7b) and propagate across the Pacific Ocean along the equatorward side of the Pacific jet. Between day -4 and day -2, Rossby wave nodes track northward toward the west coast of North America, near the coast of southern Alaska and British Columbia, Canada. Correlations are maximized on day 0, and indicate that precipitation is again positively correlated with southerly wind anomalies aloft. The predominantly southwest/northeast tilt of the Rossby wave patterns imply equatorward propagation on and after day 0. The patterns are also elongated meridionally. While the day 4 correlation map suggests a single track across the Atlantic, the results are based on averaging across models so that individual models could show more than one track downstream of Great Lakes region (Fig. 7b).

Maximum multi-model average day 0 correlations between simulated precipitation and 300 hPa meridional winds are shown in Figure 3, along with observational results. On average, the models are able to capture the seasonality of the relationship between precipitation and upper-level winds. Models produce the greatest correlations during the transition seasons (spring and autumn), with the lowest values simulated during winter. Simulated correlations are slightly higher than in observations during winter, which is likely because models are unable to simulate small-scale processes that result in observed winter precipitation in the Great Lakes region, namely lake-effect snow events. As such, winter precipitation in the GCMs shows a stronger relationship with large-scale atmospheric processes.

### *b. 300 hPa Meridional wind*

We continue to explore how simulated variations in the upper-level flow field influence transient Rossby waves that traverse the Great Lakes region using correlation maps based solely on 300 hPa meridional wind. We present a multi-model composite analysis of simulated time-lag correlation maps for the month of July to illustrate differences in Rossby wave features among models. A more objective analysis between the upper-level zonal wind field and transient Rossby waves can be found below. Composites are based on identifying models (Table 1) with above-average (Fig. 8a) and below-average (Fig. 8b) zonal wind component at 300 hPa within the eastern fringe of the North Pacific extratropical jet (40°-52.5°N, 180°-150°W; black box in Fig. 8a, b), where above- and below-average are relative to the multi-model mean. There are eight models in each composite. The above- (below-) average composite represents an elongated and stronger (contracted and weaker) extratropical Pacific jet.

Composites in Fig. 8a indicate that models with above-average zonal wind speeds south of the Aleutian Islands are characterized by a uniform extratropical Pacific jet, with relatively constant zonal wind from the east coast of China to the west coast of North America. Average zonal wind speeds in the eddy-driven Atlantic jet (>20 m $s^{-1}$) are stronger than the Pacific jet (10-15 m $s^{-1}$). Zonal wind speeds in the above-average composite are greater than the reanalysis data (Fig. 8c) in the latitude band between 20°N and 45°N. Average simulated zonal wind speeds are lower over the northeastern North Pacific, across the western half of Canada (near 50°N), and over the North Atlantic, between western North America and eastern Europe (55°-60°N). On average, simulated Rossby wave trains in the above-average pool of models originate over eastern Asia and western North Pacific (day -6) and propagate along the extratropical jet stream with little meridional deviation from day -6 to day 0.

Models with below-average zonal wind speeds south of the Aleutian Islands produce differing results. The multi-model average 300 hPa zonal wind structure is characterized by weaker zonal winds across the entire extratropical North Pacific and North Atlantic Oceans, as compared to the above-average composite. The Pacific jet appears disconnected from the jet over central Canada, while the multi-model average includes a relatively weak (<10 m $s^{-1}$) subtropical jet located off southwest coast of North America, a feature that is absent in the above-average composite. Relative to reanalysis data (Fig. 8c), zonal winds in the below-average composite are weaker in the core of the observed Pacific and Atlantic jets by 7 and 4 m $s^{-1}$, respectively. The below-average composite shows subtropical zonal winds south of 30°N that are stronger than in the reanalysis data across most of the domain presented in Fig. 8b. Unlike observations and the above-average composite, simulated Rossby wave trains in these models show, on average, two preferred origins: the tropical North Pacific Ocean, south of the Hawaiian islands (day -6), and the central North Pacific Ocean (day -4). The two paths merge over the eastern North Pacific Ocean and propagate as a single wave train across North America.

July time-lag correlation maps based on the NCEP-NCAR Reanalysis data (Fig. 8c) indicate the transient Rossby waves that traverse the Great Lakes region originate over the western North Pacific Ocean (day -4) and propagate across North America (day -2) and the

North Atlantic (day 0), within the eddy-driven jets. The wave structure shows little sign of subtropical or tropical origin.

The July composite analysis suggests that the climatological structure of the 300 hPa zonal wind field influences the origin and propagation path of transient Rossby waves that traverse the Upper Midwest in 20th century GCM simulations. However, potential differences in the phase of waves due to differences in wavelength among models may limit the robustness of such composites. In fact, close inspection of individual time-lag correlation maps indicates that differences in zonal and meridional wavelengths exist among the CMIP3 models, ultimately impacting wave phase. Consequently, averaging correlation fields that contain positive and negative features across different models will likely reduce the amplitude of resulting waves. To avoid this, the Hilbert transform is applied to each model's time-lag correlation maps to identify and track the Rossby Wave Envelopes (RWEs). The Hilbert transform of a real array, $x_r$, returns a real array, $x_h$, that is the original data where each wave number is phase shifted by 90° (Ouergli 2002; Strong and Liptak 2012). The returned array, $x_h$, has the same frequency and amplitude as the original data, $\mathrm{x}_r$. The wave envelope is identified by calculating the square root of the sum of the squared real component and phase-shifted component [$x_e = \sqrt{x_r^2 + x_h^2}$]. The units and scale of the resulting array, $x_e$, are the same as the original time series (correlation coefficients), and values are all greater than or equal to zero, thereby eliminating concern of wave cancellation. In the current analysis, the Hilbert transform is applied to spatial correlation maps and represents a *proxy* for Rossby wave activity, which is not to be confused with the dynamical definition of wave activity (e.g. Plumb 1986). The Hilbert transform was previously applied in space by Zimin et al. (2003), Danielson et al. (2006), Ambaum and Athanasiadis (2007), and Ambaum (2008).

An example of the Hilbert transform applied to observed time-lag correlation maps (Fig. 4b) demonstrates the effect on the Rossby wave train. As described above, the observed time-lag correlation maps for April (Fig. 4a) indicate the Rossby wave train originates over eastern Asia and propagates along the extratropical Pacific jet from day -4 to day -2. Beyond day -2, the leading nodes expand meridionally and follow two possible tracks, a northern track propagating along the eddy-driven Atlantic jet and a southern track propagating toward the west coast of Africa. The RWEs identified using the Hilbert transform (Fig. 4b) capture the spatial extent of the Rossby wave train as it propagates eastward along the extratropical jets and into the tropics. By day +2, the RWE captures a regional maximum over the tropical North Atlantic (~15°N) and off the east coast of North America (~45°N), corresponding to the two tracks previously mentioned. Thus, the RWEs in Fig. 4b, in conjunction with previous applications (Zimin et al. 2003; Ambaum and Athanasiadis 2007), suggest the Hilbert transform is a useful tool for approximating the location and propagation of transient Rossby wave trains.

Rather than repeating the composite analysis using RWEs, we expand our analysis to further illustrate how simulated variations in the background flow are related to variations in Rossby waves using Maximum Covariance Analysis (MCA). MCA, sometimes referred to as Singular Value Decomposition, is a statistical technique used to identify patterns of covariability between time series of two different variables (Bretherton et al. 1992; Wallace et al. 1992). MCA involves calculating a covariance matrix between two variables over a sampling dimension. In the current analysis, we evaluate patterns of covariability between model-simulated mean 300 hPa zonal winds and model-simulated day -3 RWEs within the region bounded by 110°E-300°E, 0°-70°N, the Pacific-North American region. MCA was repeated using a number of smaller 300 hPa zonal wind domains, which resulted in very little change to the dominant patterns of covariability and statistical significance, thereby verifying the robustness of our findings. Day -3 RWEs are chosen to emphasize differences in upstream characteristics of simulated Rossby wave trains among models. Before computing the covariance matrix, the multi-model mean of both variables is removed, and both variables are weighted by the square root of the cosine of latitude.

Unlike most MCA studies (Bretherton et al. 1992; Deser and Timlin 1997), the covariance matrix is calculated over the model dimension (16 GCMs), rather than the time dimension, for each month separately. This is similar to the approach applied by Delcambre et al. (2013a,b). Because the current MCA analysis samples across model space rather than time, identified patterns are not equivalent to temporal variability of any single model. Instead, the patterns represent inter-model variability of climatological 300 hPa zonal wind speed anomalies that are associated with day -3 RWE anomalies. MCA results for the leading mode of covariability are presented in the form of heterogeneous regression patterns, in which model-simulated 300 hPa zonal wind speed is regressed onto the day -3 RWE expansion coefficients and model-simulated day -3 RWEs are regressed onto the 300 hPa zonal wind expansion coefficients. MCA results for two contrasting months, July and December, are presented to illustrate differences in the influence of the basic-state on transient Rossby waves.

The strength of coupling between the two (left and right) heterogeneous regression patterns for each month is measured by the squared covariance fraction (SCF) and the normalized squared covariance (NSC) (Table 2). The SCF, defined by Bretherton et al. (1992), represents the amount of covariance explained by each mode, though we present results for the first mode only. Values range from a minimum of 46% in March to a maximum of 73% in November. The NSC corresponds to the ratio between the squared covariance represented by the first mode and the square-root of the product of the area-integrated variance in the two fields (Wallace et al. 1992; Santos et al. 2007). Wallace et al. (1992) suggest that NSC values above 0.1 represent strong coupling, although large values of NSC combined with small values of shared covariance likely have little meaning. Monthly values of the NSC (Table 2) range from 0.28 in April to 0.38 in September. The significance of the correlations between the left and right expansion coefficients (Table 2) was tested using a Monte Carlo approach, in which the left and right fields were randomly paired before computing the covariance matrix. We performed 1000 random iterations for each month. Significant correlations based on the 95th percentile of the Monte Carlo correlation distribution include nine of the 12 months and are shown in bold in Table 2. Finally, the amount of variance among models explained by each of the heterogeneous regression patterns is shown in the two rightmost columns of Table 2.

MCA results for July (Fig. 9c,d) indicate that models characterized by above-average 300 hPa zonal wind speeds across the extratropical North Pacific and United States (30-45°N), concurrent with slightly below-average zonal wind speeds in the subtropical North Pacific (15-25°N), are associated with above average Rossby wave activity over the North Pacific. The RWE anomaly pattern represents a westward expansion of the multi-model maximum located off the northwest coast of North America (Fig. 9b). Conversely, models with slightly above average zonal wind speeds across the subtropical North Pacific and below average zonal wind speeds across the extratropical North Pacific and United States are accompanied by above-average Rossby wave activity emanating from the central tropical Pacific and below-average wave activity upstream of the multi-model maximum on day -3. These results, which agree with the multi-model July composites (Fig. 8a,b), suggest that stronger winds in the extratropical jet tend to increase the strength of the extratropical waveguide. Wave activity over the Great Lakes region is, therefore, more likely to originate in the Pacific jet in this case. Conversely, in the presence of weaker winds in the extratropical jet, the extratropical waveguide is weakened and therefore, wave activity over the Great Lakes tends to trace a more great-circle-like path that originates in the tropical Pacific. The tropical versus extratropical origin of simulated Rossby wave activity is not unique to July, but also exists during August (not shown). The statistical significance of the heterogeneous regression patterns shown in Figure 9c and 9d was determined using a Monte Carlo approach. Left and right patterns were randomly paired for each month separately, and MCA was performed on each shuffled covariance matrix. This was done 1000 separate times. Thresholds for the 97.5 and 2.5 percentiles of the left and right heterogeneous patterns were obtained at each grid cell separately. Values outside of the 97.5 and 2.5 percentiles are statistically significant and are indicated by the crosses in Figure 9c, d and Figure 10c, d.

December MCA results differ from summer findings, yet closely resemble the patterns identified during November, January, and February. The December heterogeneous zonal wind pattern (Fig. 10c) indicates that models with above-average zonal wind speeds across the subtropics, including above-average zonal winds in the Pacific jet entrance and exit regions, and reduced wind speeds to the north and south of the subtropical belt, are associated with increased wave activity emanating from the tropical central Pacific Ocean and less wave activity in the western Pacific jet stream (Fig. 10d).

The expansion coefficient from a single model for one of the two input variables represents the amplitude of the projection of that model's anomaly pattern (relative to the multi-model mean) onto the corresponding heterogeneous regression pattern, for each month separately. High correlation values between left and right expansion coefficients (i.e. the left and right singular vectors) indicate a high degree of coupling between the patterns identified, increasing the confidence in MCA results (Delcambre et al. 2013a). A scatterplot of expansion coefficients, including a point for the reanalysis data, is presented in Figure 11 based on results from July and December. A data point for the reanalysis data is also included in each subplot (red triangle), showing the projection of the average reanalysis field minus the multi-model mean (similar to all other points) onto the corresponding heterogeneous regression pattern from the MCA results. For example, the July x-value for the reanalysis data in Figure 11 represents the projection of average July 300 hPa zonal winds (Fig. 8c) minus the multi-model average (Fig. 9a) projected onto the heterogeneous pattern in Figure 9c.

In July, the expansion coefficients based on the reanalysis data fall very close to the middle of the GCM distribution. This indicates that the observed 300 hPa zonal wind field and day -3 RWE field are very close to the corresponding multi-model average fields. Removing the multi-model mean from both observed fields results in near-zero projection of the remaining data onto the heterogeneous patterns during July. Results for December follow similar logic, though the projection of observed 300 hPa zonal wind anomalies onto the heterogeneous pattern falls below zero. This finding suggests less agreement between the multi-model average fields and reanalysis fields during December, as compared to July.

Nevertheless, the observed December point is within the model scatter. This result suggests that the model biases in the background state and Rossby wave trains are related, and, moreover, that correcting biases in the mean state will also correct biases in the propagation of Rossby wave trains.

Composites of July and December 300 hPa zonal wind and day -3 RWE anomalies are presented for in Figure 12 using a subset of models that are indicated by black triangles in Figure 11. These models (three from July and two from December) are selected because their expansion coefficients are located on the extreme positive end of the distributions shown in Figure 11. The zonal wind and RWE composites for these "extreme" climate models are very similar to the patterns from MCA. This suggests that a single, dominant pattern rules the model-to-model variability in the background flow and Rossby wave propagation.

To determine whether differences in the background state are in fact causing differences in the wave propagation, we integrate the linearized barotropic vorticity equation (1) backward in time for three days, starting from the lag 0 regression map. The model is linearized about three different background states. The first background state used is the latitudinally- and longitudinally-varying rotational [2] component of the multi-model mean zonal and meridional wind, while the second and third background states are the multi-model mean wind plus or minus the winds regressed on the zonal wind expansion coefficient (i.e. plus or minus the anomalous left MCA pattern). The initial condition for the streamfunction is calculated from the meridional wind regression pattern at lag 0 under the assumption that all of the flow is rotational. The linearized barotropic equation is standard, except for the fact that the sign of the diffusion is reversed so that small scale features that develop are removed when the model is run *backwards*:

$$\frac{\partial \zeta}{\partial t} + \frac{U}{a\cos(\theta)}\frac{\partial \zeta}{\partial \lambda} + \frac{V}{a}\frac{\partial \zeta}{\partial \theta} + \frac{u}{a\cos(\theta)}\frac{\partial Z}{\partial \lambda} + \frac{v}{a}\frac{\partial (f+Z)}{\partial \theta} + \nu \nabla^2 \zeta = 0 \tag{1}$$

[2] In other words, given the meridional wind regression pattern, the zonal wind initial condition is the zonal wind that makes the total flow precisely non-divergent.

where $\zeta$, $u$ and $v$ are the wave relative vorticity, zonal wind and meridional wind, respectively, $Z$, $U$ and $V$ are the background relative vorticity, zonal wind and meridional wind, respectively, $\lambda$ is the longitude, $\theta$ is the latitude, $a$ is the radius of the earth, $f$ is the Coriolis parameter and $\nu$ is the diffusivity. Note that the vorticity equation above only involves the absolute/relative vorticity and not the potential vorticity. We believe that the absolute vorticity is more relevant because the waves are likely better described as equivalent barotropic external Rossby waves (Held et al. 1985). The propagation of external Rossby waves is governed by the winds and absolute vorticity at the "equivalent barotropic level" in the mid- to upper-troposphere (Held et al. 1985). We find that a better simulation is achieved if the background state is taken from the 400 hPa instead of the 300 hPa level. This is in better agreement with the equivalent barotropic level calculated from the Northern Hemisphere background state (Held et al. 1985). Since the meridional wind regression pattern at 400 hPa is essentially proportional to the regression pattern at 300 hPa, and the model is linear in the waves, we simply use the 300 hPa lag 0 regression map as the initial condition to predict the 300 hPa lag -3 regression map. The model resolution is T63 and the time step is 18 minutes using a third order Adams-Bashforth scheme. The value of the diffusivity is such that the smallest resolved wave is damped with an $e$-folding time of six hours. The model is integrated backwards in time for three days and the resulting meridional wind is first normalized by the local meridional wind standard deviation to allow a direct comparison to the correlation maps. Finally, the normalized meridional wind is used to calculate the RWE in the same way as in the model diagnostics described above.

The RWE at day -3 for the model-mean background flow is shown for July (Fig. 13a) and December (Fig. 13b). These figures should be compared with Fig. 9b and Fig. 10b, respectively. For July, the location and amplitude of the modelled RWE peak generally agree with the average climate model RWE, although the modelled RWE has a second relatively weak maximum southeast of the main peak that is not present in the climate models. For December, the modelled RWE has two main peaks: one in the northeast Pacific and one in the western Pacific, much like the climate models. Like July, however, the modelled RWE has an additional relatively weak maximum in the southeast Pacific that is not present in the climate models. The amplitude of the modelled RWE in December is also too large, but we believe the spatial patterns are more important because the amplitude can be adjusted by simply changing the diffusivity in the model.

To produce a result analogous to the MCA results, we take half the difference between the modelled simulation with the background from the model mean winds *plus* the anomalous MCA winds and the simulation with the background from the model mean winds *minus* the anomalous MCA winds. Differences in the RWE for July and December are shown in Fig. 13c and 13d, respectively. These figures should be compared with Fig. 9d and Fig. 10d. For July, the modelled RWE difference pattern shows positive anomalies in the central Pacific and negative anomalies further east, over the subtropical Pacific and North America. This pattern is similar to the climate model MCA pattern, except that the negative climate model pattern extends deeper into the tropics and less into northwest Canada. The disagreement between barotropic results and climate model results equatorward of 15°N suggests that model-to-model differences in this region may not be due to variations in the rotational component of the mean flow. Instead, maybe differences in this region are associated with variations in other model properties, such as tropical convection or the divergent component of the flow. For December, the modelled RWE difference pattern shows two main positive centers: one in the northeast Pacific and one in the central, subtropical Pacific. There is one main negative center in the western Pacific with a narrow tongue extending eastward to separate the two main positive centers. These features are remarkably similar to the MCA pattern from the climate models. These barotropic model simulations suggest that, to first order, changes in the background horizontal flow are responsible for the variations in wave propagation in the climate models and that differences in baroclinicity and differences in the structure of the wave packets at lag 0 are less important.

# 5. Discussion and Conclusions

In this analysis, we have expanded on previous research by exploring the direct connection between Great Lakes hydrology and large-scale atmospheric circulations. More specifically, we have examined the relationship between over-lake precipitation in the Lake Superior basin and transient Rossby waves using 300 hPa meridional winds. Observations between 1948-2010 show that over-lake precipitation in the Lake Superior basin is related to transient Rossby waves during each month of the year. The strongest correlations between over-lake precipitation estimates and 300 hPa meridional wind occur during the transition months of April and October, while the weakest correlations occur during winter months, when over-lake precipitation amounts are relatively small. Regardless of month, the instantaneous correlation maps consistently reveal a positive relationship between over-lake precipitation anomalies and an upper-level trough-ridge couplet over central North America, with positive precipitation anomalies associated with southerly winds directly overhead.

Although similarities among over-lake precipitation and meridional wind correlation maps exist, there are noticeable differences in observed Rossby wave paths throughout the year. For example, winter months are typically characterized by two different paths, both upstream over the North Pacific and downstream of the Great Lakes region, over the North Atlantic. Summer months, however, consistently produce a single path, both upstream and downstream of the Great Lakes basin. Summer disturbances propagate within the Pacific and Atlantic eddy-driven jets, or waveguides, throughout their entire life cycle. The shoulder season months represent more of a hybrid between winter and summer conditions, commonly capturing a single track upstream of the focus region and dual tracks downstream. Time-lag correlation maps between 300 hPa meridional wind at a single point (defined in relation to over-lake precipitation in the Lake Superior basin) and the 300 hPa meridional wind at all other grid cells agree well with the correlation maps based on over-lake precipitation and 300 hPa meridional wind, further supporting the influence of the mean state on transient Rossby waves.

In addition to Lake Superior relations, time-lag correlation maps were produced between over-lake precipitation estimates from the other four Great Lakes (Michigan, Huron, Erie, and Ontario) and 300 hPa meridional wind anomalies between 1948-2010 (not shown). Based on cross-correlations, the over-lake precipitation time series for the Lake Superior basin is most (least) correlated with over-lake precipitation from the Lake Michigan (Erie) basin, in agreement with the winter cross-correlations presented by Rodionov (1994). As such, the time-lag correlation maps between over-lake precipitation from the Lake Michigan basin and 300 hPa meridional winds are very similar to those presented for Lake Superior. The most noticeable differences occur during winter months (DJF), when correlations between over-lake precipitation and upper-level meridional winds are weakest for both lakes. Monthly time-lag correlation maps based on over-lake precipitation anomalies in the Lake Erie basin qualitatively resemble those for Lake Superior; however, the amplitudes are less than those observed using the Lake Superior precipitation anomalies and the meridional wavelengths of the Rossby waves are slightly smaller. Since the focus of the current study is on the Great Lakes region, further research is warranted to explore the impact of the background flow on transient waves around the globe.

Beyond observations, output from 16 CMIP3 models is analyzed to further demonstrate how variations in the simulated upper-level zonal wind field influence the origin and propagation path of transient Rossby waves that support precipitation and that traverse the central United States. Multi-model average time-lag correlation maps between simulated precipitation and 300 hPa meridional wind closely resemble the correlation maps defined solely using 300 hPa meridional wind, though correlations between precipitation and 300 hPa meridional wind are weaker.

Results from model simulations suggest that the structure of the time-mean, upper-level flow influences Rossby wave propagation across the Pacific Ocean, North America, and Atlantic Ocean, ultimately impacting the relative influence of the tropics and extratropics on the hydroclimate of the Great Lake region. Composite analysis and MCA results show that models with above-average zonal winds in the summertime extratropical jet more closely resemble the reanalysis data and show RWEs propagating along the extratropical jet, within the waveguide, both upstream and downstream of the Great Lakes region. Alternatively, models that simulate below-average zonal winds in the extratropical jet are characterized by more wave activity reaching the Great Lakes region from a tropical path, rather than originating within the extratropics. Experiments with a barotropic model linearized about the background flow reproduce the results of the MCA patterns to a remarkable degree and further support our hypothesis that changes in the background horizontal flow are responsible for the variations in the origin of wave packets, and that differences in baroclinicity and the structure of wave packets while they are over the Great Lakes region are less important.

Based on these findings, one could hypothesize that simulated tropical Pacific Ocean conditions may influence Great Lakes precipitation variability in models with weak waveguides. Because ENSO variability is more persistent than internal extratropical variability, one might further hypothesize that precipitation variability is too persistent in these models. Also, since water levels in the Great Lakes basin are integrative, lake levels are more sensitive to low-frequency precipitation variability, and downscaled lake level variability based on the weak waveguide models will be too large. These results also have possible implications to future anthropogenic climate change. The projected background flow changes under increased concentrations of greenhouse gases include a poleward shift of the extratropical jets (Lorenz and DeWeaver 2007; Delcambre et al. 2013a) and an expansion of the tropical Hadley Cell (Lu et al. 2007; Johanson and Fu 2009). The results here imply that these background state changes will affect the propagation of Rossby waves and will likely have important consequences for the water resources in the Great Lakes region.

*Acknowledgments.*

We acknowledge Tim Hunter, from NOAA's Great Lakes Environmental Research Laboratory, for providing the over-lake precipitation estimates. We acknowledge the modeling groups, the Program for Climate Model Diagnosis and Intercomparison (PCMDI), and the WCRP's Working Group on Coupled Modeling (WGCM) for their roles in making available the WCRP CMIP3 multi-model dataset. Support of this dataset is provided by the Office of Science, U.S. Department of Energy. NCEP-NCAR Reanalysis data was provided by the NOAA/OAR/ESRL PSD, Boulder, Colorado, USA, from their website at http://www.esrl.noaa.gov/psd/. We would also like to acknowledge two anonymous reviewers for their valuable insights and suggestions. This study was funded by the Michigan Department of Natural Resources through the Environmental Protection Agency Great Lakes Restoration Initiative grant. CCR publication # .

# REFERENCES

Ambaum, M., 2008: Unimodality of wave amplitude in the Northern Hemisphere. *J. Atmos. Sci.*, **65 (3)**, 1077–1086.

Ambaum, M. and P. Athanasiadis, 2007: The response of a uniform horizontal temperature gradient to heating. *J. Atmos. Sci.*, **64 (10)**, 3708–3716.

Assel, R., J. Janowiak, D. Boyce, C. O'Connors, F. Quinn, and D. Norton, 2000: Laurentian Great Lakes ice and weather conditions for the 1998 El Niño winter. *Bull. Amer. Meteor. Soc.*, **81 (4)**, 703–717.

Barnes, E. and D. Hartmann, 2011: Rossby wave scales, propagation, and the variability of eddy-driven jets. *J. Atmos. Sci.*, **68 (12)**, 2893–2908.

Branstator, G., 1983: Horizontal energy propagation in a barotropic atmosphere with meridional and zonal structure. *J. Atmos. Sci.*, **40 (7)**, 1689–1708.

Branstator, G., 1995: Organization of storm track anomalies by recurring low-frequency circulation anomalies. *J. Atmos. Sci.*, **52 (2)**, 207–226.

Branstator, G., 2002: Circumglobal teleconnections, the jet stream waveguide, and the North Atlantic Oscillation. *J. Climate*, **15 (14)**, 1893–1910.

Bretherton, C., C. Smith, and J. Wallace, 1992: An intercomparison of methods for finding coupled patterns in climate data. *J. Climate*, **5 (6)**, 541–560.

Chang, E., 1993: Downstream development of baroclinic waves as inferred from regression analysis. *J. Atmos. Sci.*, **50 (13)**, 2038–2053.

Chatterjee, P. and B. N. Goswami, 2004: Structure, genesis and scale selection of the tropical quasi-biweekly mode. *Quarterly J. of the Roy. Meteo. Soc.*, **130 (599)**, 1171–1194.

Coleman, J. and J. Rogers, 2003: Ohio River Valley winter moisture conditions associated with the Pacific-North American teleconnection pattern. *J. Climate*, **16 (6)**, 969–981.

Croci-Maspoli, M., C. Schwierz, and H. Davies, 2007: A multifaceted climatology of atmospheric blocking and its recent linear trend. *J. Climate*, **20 (4)**, 633–649.

Croley, T. and H. Hartmann, 1985: Resolving Thiessen polygons. *J. Hydrology*, **76 (3-4)**, 363–379.

Croley, T. and T. Hunter, 1994: Great Lakes Monthly Hydrologic Data. *NOAA Technical Memorandum ERL GLERL-83*.

Danielson, R., J. Gyakum, and D. Straub, 2006: A case study of downstream baroclinic development over the North Pacific Ocean. Part II: Diagnoses of eddy energy and wave activity. *Mon. Wea. Rev.*, **134 (5)**, 1549–1567.

Delcambre, S. C., D. Lorenz, D. Vimont, and J. Martin, 2013a: Diagnosing Northern Hemisphere jet portrayal in 17 CMIP3 global climate modesl: Twentieth century inter-model variability. *J. Climate*, **26**, 4910–4929.

Delcambre, S. C., D. Lorenz, D. Vimont, and J. Martin, 2013b: Diagnosing Northern Hemisphere jet portrayal in 17 CMIP3 global climate modesl: Twenty-first century projections. *J. Climate*, **26**, 4930–4946.

Deser, C. and M. Timlin, 1997: Atmosphere-ocean interaction on weekly timescales in the North Atlantic and Pacific. *J. Climate*, **10 (3)**, 393–408.

Ding, Q. and B. Wang, 2005: Circumglobal teleconnection in the Northern Hemisphere summer*. *J. Climate*, **18 (17)**, 3483–3505.

Feldstein, S. and U. Dayan, 2008: Circumglobal teleconnections and wave packets associated with Israeli winter precipitation. *Q. J. R. Meteorol. Soc.*, **134 (631)**, 455–467.

Fujinami, H. and T. Yasunari, 2009: The effects of midlatitude waves over and around the Tibetan Plateau on submonthly variability of the East Asian summer monsoon. *Mon. Wea. Rev.*, **137 (7)**, 2286–2304.

Ghanbari, R. and H. Bravo, 2008: Coherence between atmospheric teleconnections, Great Lakes water levels, and regional climate. *Adv. in Wat. Res.*, **31 (10)**, 1284–1298.

Grover, E. and P. Sousounis, 2002: The influence of large-scale flow on fall precipitation systems in the Great Lakes Basin. *J. Climate*, **15 (14)**, 1943–1956.

Hakim, G., 2003: Developing wave packets in the North Pacific storm track. *Mon. Wea. Rev.*, **131 (11)**, 2824–2837.

Hanrahan, J., S. Kravtsov, and P. Roebber, 2010: Connecting past and present climate variability to the water levels of Lakes Michigan and Huron. *Geo. Res. Lett.*, **37 (1)**, L01 701.

Held, I., 1983: Stationary and quasi-stationary eddies in the extratropical troposphere: Theory. *Large-Scale Dynamical Processes in the Atmosphere*, B. J. Hoskins and R. P. Pearce, Eds., Academic Press, 127–168.

Held, I. M., R. L. Panetta, and R. T. Pierrehumbert, 1985: Stationary external Rossby waves in vertical shear. *J. Atmos. Sci.*, **42 (9)**, 865–883.

Holman, K., A. Gronewold, M. Notaro, and A. Zarrin, 2012: Improving historical precipitation estimates over the Lake Superior basin. *Geo. Res. Lett.*, **39 (3)**, L03 405.

Holman, K. and S. Vavrus, 2012: Understanding simulated extreme precipitation events in Madison, Wisconsin and the role of moisture flux convergence during the late 20th and 21st centuries. *J. Hydrometeor.*, **13 (3)**, 877–894.

Hoskins, B. and T. Ambrizzi, 1993: Rossby wave propagation on a realistic longitudinally varying flow. *J. Atmos. Sci.*, **50 (12)**, 1661–1671.

Hoskins, B. and D. Karoly, 1981: The steady linear response of a spherical atmosphere to thermal and orographic forcing. *J. Atmos. Sci.*, **38 (6)**, 1179–1196.

Hoskins, B., A. Simmons, and D. Andrews, 1977: Energy dispersion in a barotropic atmosphere. *Quarterly J. of the Roy. Meteo. Soc.*, **103 (438)**, 553–567.

Hovmöller, E., 1949: The Trough-and-Ridge diagram. *Tellus*, **1 (2)**, 62–66.

Isard, S., J. Angel, and G. VanDyke, 2000: Zones of origin for Great Lakes cyclones in North America, 1899-1996. *Mon. Wea. Rev.*, **128 (2)**, 474–485.

Johanson, C. and Q. Fu, 2009: Hadley cell widening: Model simulations versus observations. *J. Climate*, **22 (10)**, 2713–2725.

Kalnay, E., et al., 1996: The NCEP/NCAR 40-year reanalysis project. *Bull. Amer. Meteor. Soc.*, **77 (3)**, 437–471.

Karoly, D., 1983: Rossby wave propagation in a barotropic atmosphere. *Dyn. of Atm. and Ocn.*, **7 (2)**, 111–125.

Knippertz, P., 2005: Tropical-extratropical interactions associated with an Atlantic tropical plume and subtropical jet streak. *Mon. Wea. Rev.*, **133 (9)**, 2759–2776.

Kosaka, Y., H. Nakamura, M. Watanabe, and M. Kimoto, 2009: Analysis on the dynamics of a wave-like teleconnection pattern along the summertime Asian jet based on a reanalysis dataset and climate model simulations. *J. of the Meteo. Soc. of Japan*, **87 (3)**, 561–580.

Kushner, P., I. Held, and T. Delworth, 2001: Southern Hemisphere atmospheric circulation response to global warming. *J. Climate*, **14 (10)**, 2238–2249.

Lee, S. and I. Held, 1993: Baroclinic wave packets in models and observations. *J. Atmos. Sci.*, **50 (10)**, 1413–1428.

Lenters, J., 2004: Trends in the Lake Superior water budget since 1948: A weakening seasonal cycle. *J. of Great Lakes Res.*, **30 (1)**, 20–40.

Lim, G. H. and J. M. Wallace, 1991: Structure and evolution of baroclinic waves as inferred from regression analysis. *J. Atmos. Sci.*, **48 (15)**, 1718–1732.

Lorenz, D. and E. DeWeaver, 2007: Tropopause height and zonal wind response to global warming in the IPCC scenario integrations. *J. of Geo. Res.*, **112 (D10)**, D10 119.

Lu, J., G. Vecchi, and T. Reichler, 2007: Expansion of the Hadley cell under global warming. *Geophys. Res. Lett.*, **34 (6)**, L06 805.

Martius, O., C. Schwierz, and H. Davies, 2008: Far-upstream precursors of heavy precipitation events on the Alpine south-side. *Quarterly J. of the Roy. Meteo. Soc.*, **134**, 417–428.

Martius, O., C. Schwierz, and H. Davies, 2010: Tropopause-level waveguides. *J. Atmos. Sci.*, **67 (3)**, 866–879.

Matthews, A., 2000: Propagation mechanisms for the Madden-Julian Oscillation. *Quarterly J. of the Roy. Meteo. Soc.*, **126 (569)**, 2637–2651.

Meehl, G., C. Covey, T. Delworth, M. Latif, B. McAvaney, J. Mitchell, R. Stouffer, and K. Taylor, 2007: The WCRP CMIP3 multi-model dataset: A new era in climate change research. *Bull. Amer. Meteor. Soc.*, **88**, 1383–1394.

Newman, M. and P. Sardeshmukh, 1998: The impact of the annual cycle on the North Pacific/North American response to remote low-frequency forcing. *J. Atmos. Sci.*, **55 (8)**, 1336–1353.

Norton, D. and S. Bolsenga, 1993: Spatiotemporal trends in lake effect and continental snowfall in the Laurentian Great Lakes, 1951-1980. *J. Climate*, **6 (10)**, 1943–1956.

Notaro, M., W. Wang, and W. Gong, 2006: Model and observational analysis of the northeast US regional climate and its relationship to the PNA and NAO patterns during early winter. *Mon. Wea. Rev.*, **134**, 3479–3505.

Notaro, M., A. Zarrin, S. Vavrus, and V. Bennington, 2013: Simulation of heavy lake-effect snowstorms across the Great Lakes Basin by RegCM4: Synoptic climatology and variability. *Mon. Wea. Rev.*, **141**, 1990–2014.

Opsteegh, J. and H. Van den Dool, 1980: Seasonal differences in the stationary response of a linearized primitive equation model: Prospects for long-range weather forecasting?. *J. Atmos. Sci.*, **37**, 2169–2185.

Ouergli, A., 2002: Hilbert transform from wavelet analysis to extract the envelope of an atmospheric mode: Examples. *J. of Atmos. and Oceanic Technol.*, **19 (7)**, 1082–1086.

PCMDI, 2007: CMIP3 Climate Model Documentation, References, and Links. Retrieved on March 1, 2014. `http://www-pcmdi.llnl.gov/ipcc/model_documentation/ipcc_model_documentation.php`.

Plumb, R., 1986: Three-dimensional propagation of transient quasi-geostrophic eddies and its relationship with the eddy forcing of the time-mean flow. *J. Atmos. Sci.*, **43 (16)**, 1657–1678.

Rodionov, S., 1994: Association between winter precipitation and water level fluctuations in the Great Lakes and atmospheric circulation patterns. *J. Climate*, **7 (11)**, 1693–1706.

Rodionov, S. and R. Assel, 2000: Atmospheric teleconnection patterns and severity of winters in the Laurentian Great Lakes basin. *Atmos.-Ocean*, **38 (4)**, 601–635.

Rogers, J. and J. Coleman, 2003: Interactions between the Atlantic Multidecadal Oscillation, El Niño/La Niña, and the PNA in winter Mississippi valley stream flow. *Geophys. Res. Lett*, **30 (10)**, 1518.

Santos, J., J. Corte-Real, U. Ulbrich, and J. Palutikof, 2007: European winter precipitation extremes and large-scale circulation: A coupled model and its scenarios. *Theo. and App. Clim.*, **87 (1)**, 85–102.

Schwierz, C., S. Dirren, and H. Davies, 2004: Forced waves on a zonally aligned jet stream. *J. Atmos. Sci.*, **61 (1)**, 73–87.

Strong, C. and J. Liptak, 2012: Propagating atmospheric patterns associated with Midwest winter precipitation. *J. Hydrometeor.*, **13 (4)**, 1371–1382.

Wallace, J., C. Smith, and C. Bretherton, 1992: Singular value decomposition of wintertime sea surface temperature and 500-mb height anomalies. *J. Climate*, **5 (6)**, 561–576.

Wang, S., L. Hipps, R. Gillies, X. Jiang, and A. Moller, 2010: Circumglobal teleconnection and early summer rainfall in the US Intermountain West. *Theo. and App. Clim.*, **102 (3)**, 245–252.

Webster, P. and J. Holton, 1982: Cross-equatorial response to middle-latitude forcing in a zonally varying basic state. *J. Atmos. Sci.*, **39 (4)**, 722–733.

Yun, K., S. Kim, K. Ha, and M. Watanabe, 2011: Effects of subseasonal basic state changes on Rossby wave propagation during northern summer. *J. Geo. Res.*, **116 (D24)**, D24 102.

Zimin, A., I. Szunyogh, D. Patil, B. Hunt, and E. Ott, 2003: Extracting envelopes of Rossby wave packets. *Mon. Wea. Rev.*, **131 (5)**, 1011–1017.

# List of Tables

TABLE 1. Coupled ocean-atmosphere GCMs from the CMIP3 (Meehl et al. 2007). Models from the above-average July composite (Fig. 8a) are indicated by (*).

| | Institute | Model | Resolution |
|---|---|---|---|
| 1 | Canadian Centre for Climate Modeling & Analysis | CGCM3.1(T47)* | T47 |
| 2 | Canadian Centre for Climate Modeling & Analysis | CGCM3.1(T63)* | T63 |
| 3 | Meteo-France / Centre National de Recherches Meteorologiques | CNRM-CM3 | T42 |
| 4 | CSIRO Atmospheric Research | CSIRO Mk3.0 | T42 |
| 5 | CSIRO Atmospheric Research | CSIRO Mk3.5 | T63 |
| 6 | US Dept. of Commerce, NOAA, Geophysical Fluid Dynamics Laboratory | GFDL CM2.0* | $2.5° \times 2.5°$ |
| 7 | NASA, Goddard Institute for Space Studies | GISS-AOM* | $4° \times 3°$ |
| 8 | NASA, Goddard Institute for Space Studies | GISS-ER | $4° \times 3°$ |
| 9 | Institute for Applied Physics | IAP FGOALS-g1.0 | $2.8° \times 2.8°$ |
| 10 | Instituto Nazionale di Geofisica e Vulcanologia | INGV-ECHAM4 | T42 |
| 11 | Institute for Numerical Mathematics | INM-CM3.0 | $5° \times 5°$ |
| 12 | Center for Climate System Research (The University of Tokyo), National Institute for Environmental Studies, and Frontier Research Center for Global Change (JAMSTEC) | MIROC3.2(hires) | T106 |
| 13 | Center for Climate System Research (The University of Tokyo), National Institute for Environmental Studies, and Frontier Research Center for Global Change (JAMSTEC) | MIROC3.2(medres) | T42 |
| 14 | Meteorological Institute of the University of Bonn, Meteorological Research Institute of KMA, and Model and Data group | MIUB* | $4.0° \times 3.75°$ |
| 15 | Max Planck Institute for Meteorology | MPI-ECHAM5-OM* | T63 |
| 16 | Meteorological Research Institute | MRI-CGCM2.3.2* | T42 |

Table 2. Squared covariance fraction (SCF), normalized squared covariance (NSC), the correlation coefficient (r) between the 300 hPa zonal wind (left) and RWE (right) expansion coefficients for the leading mode of covariability, 300 hPa u-wind variance among models explained by the heterogeneous pattern (U Var), and Day -3 RWE variance among models explained by the heterogeneous pattern (RWE Var). Bold correlations are significant at the 95% confidence interval based on 1000 Monte Carlo simulations.

| Month | SCF (%) | NSC | r(left,right) | U Var (%) | RWE Var (%) |
|---|---|---|---|---|---|
| Jan | 58 | 0.33 | **0.93** | 27 | 19 |
| Feb | 59 | 0.30 | 0.82 | 25 | 16 |
| Mar | 46 | 0.30 | **0.90** | 32 | 11 |
| Apr | 49 | 0.28 | 0.81 | 19 | 15 |
| May | 53 | 0.31 | 0.83 | 20 | 17 |
| Jun | 63 | 0.32 | **0.91** | 24 | 22 |
| Jul | 63 | 0.32 | **0.90** | 21 | 26 |
| Aug | 47 | 0.31 | **0.93** | 18 | 22 |
| Sep | 67 | 0.38 | **0.88** | 24 | 37 |
| Oct | 60 | 0.34 | **0.92** | 25 | 23 |
| Nov | 73 | 0.36 | **0.90** | 30 | 25 |
| Dec | 63 | 0.37 | **0.94** | 32 | 26 |

# List of Figures

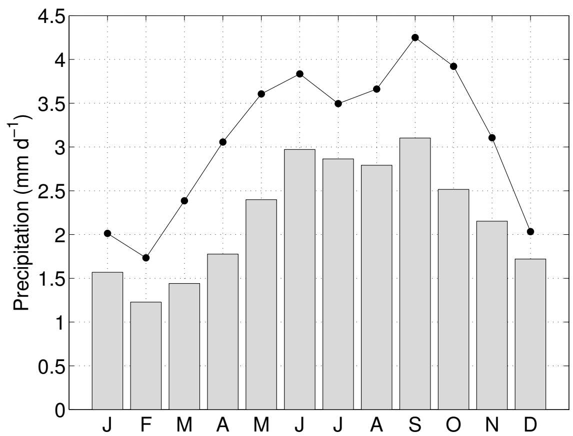


FIG. 1. Average monthly estimates of over-lake precipitation (mm d$^{-1}$; bars) and associated monthly standard deviation (mm d$^{-1}$; line) in the Lake Superior basin between 1948-2010 based on estimates from NOAA's Great Lakes Environmental Research Laboratory.

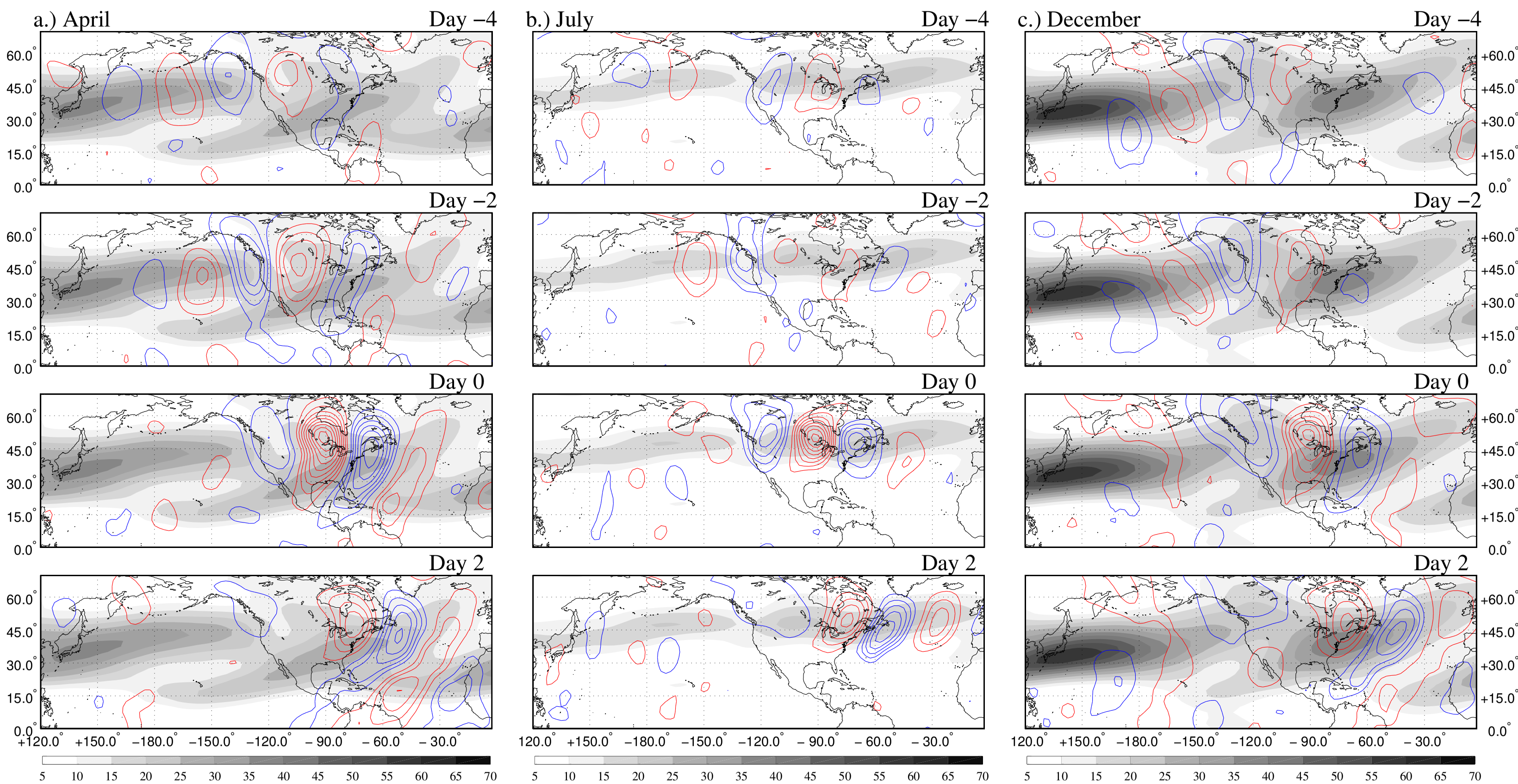


FIG. 2. Time-lag correlation maps (contours) between daily over-lake precipitation anomalies and observed 300 hPa meridional wind anomalies during (a) April, (b) July, and (c) December for four different lead/lag values. Negative (positive) lag values indicate the meridional wind anomalies precede (follow) the over-lake precipitation anomalies. The contour interval is 0.05, with positive (negative) correlations shown in red (blue) and the zero line is omitted. Correlation values greater/less than $\pm$ 0.04 are significant at the 95% confidence level, based on the Student's two-tailed t-test, where the degrees of freedom are scaled by the autocorrelation of precipitation. Shading indicates average monthly 300 hPa zonal wind speed (m $s^{-1}$) between 1948-2010.

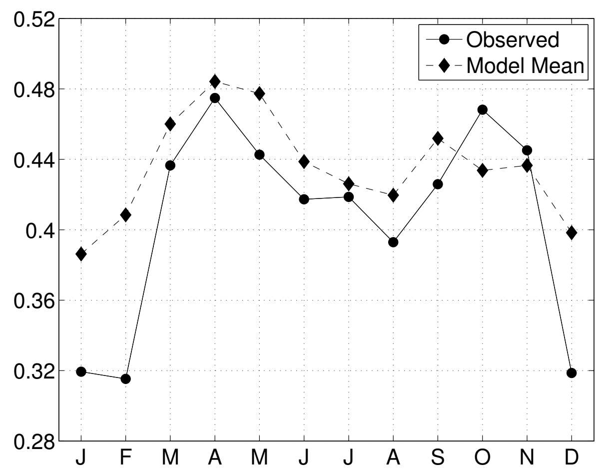


FIG. 3. Maximum zero-lag correlation between daily over-lake precipitation anomalies in the Lake Superior basin and 300 hPa meridional wind anomalies within the domain 120°E-360°W, 0°-70°N, for each month separately based on observations between 1948-2010 (solid line with circles) and model simulations between 1961-2000 (dashed line with diamonds). Simulated precipitation anomalies are based on averaging the precipitation in the grid cell closest to Lake Superior, 48°N, 272°E, and the two adjacent grid cells together. All observed correlations are statistically significant at the 95% confidence interval based on the Student's two-tailed t-test.

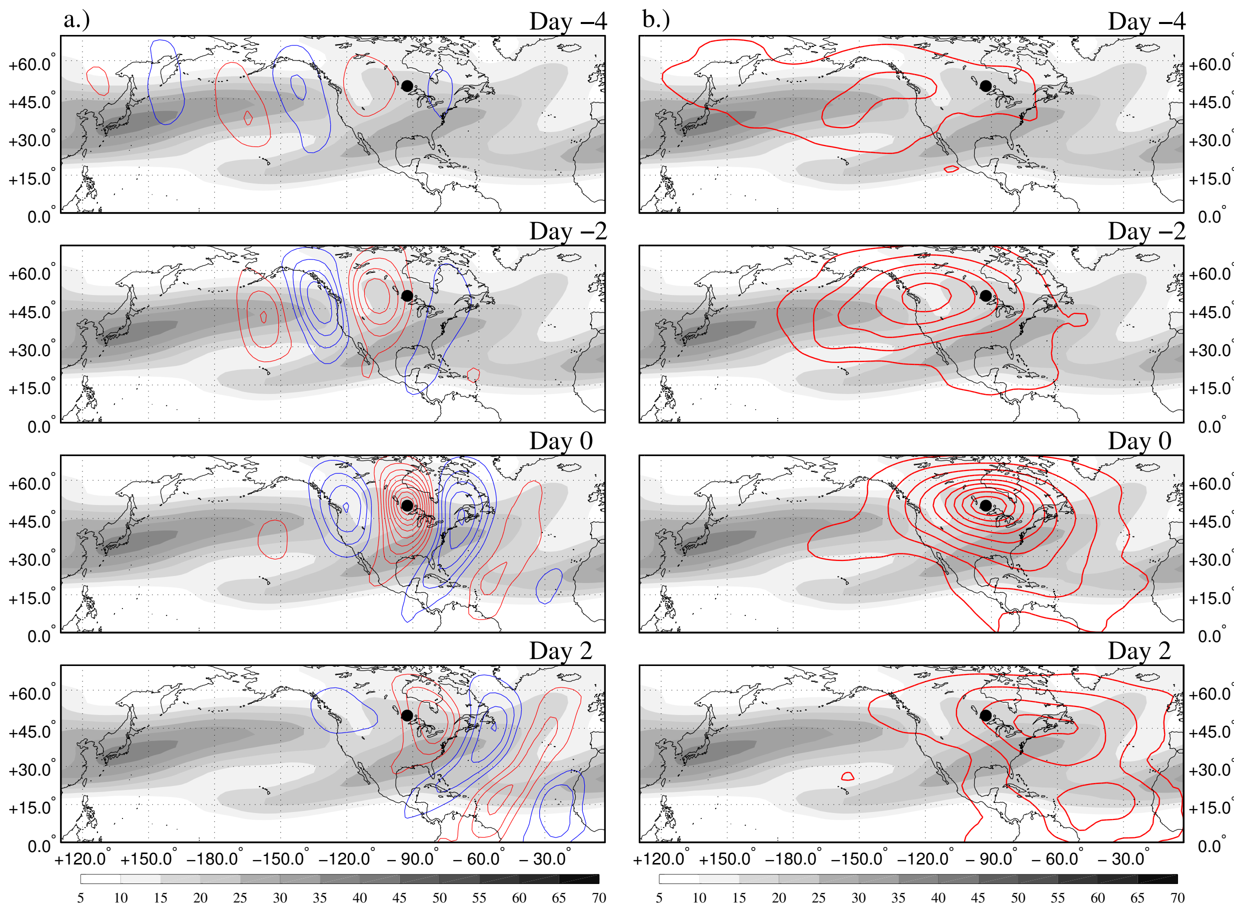


FIG. 4. (a) Time-lag correlation maps between daily 300 hPa meridional wind anomalies at 50.0°N, 267.5°E (black dot) and 300 hPa meridional wind anomalies at each grid cell during all Aprils between 1948-2010 based on NCEP-NCAR Reanalysis data. Positive (negative) correlations are shown in red (blue). (b) Rossby Wave Envelope (RWE) of time-lag correlation maps in (a) calculated using the Hilbert transform (Ouergli 2002). Negative (positive) lag values indicate the meridional wind anomalies precede (follow) the base point. Contour interval is 0.1 with the zero line omitted. Shading indicates the climatological April 300 hPa zonal wind (m $s^{-1}$) between 1948-2010.

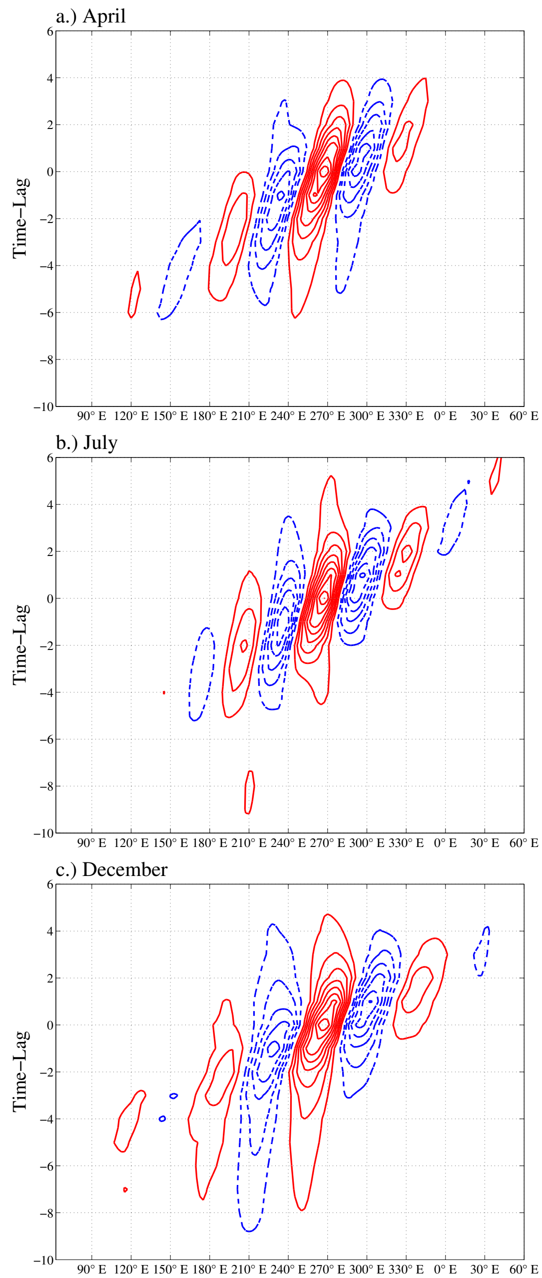


FIG. 5. Hovmöller diagram displaying the correlation between observed daily 300 hPa meridional wind anomaly time series at 50.0°N, 267.5°E and daily 300 hPa meridional wind anomalies averaged over 35°N-55°N during (a) April, (b) July, and (c) December, between 1948-2010. The vertical axis represents the lag value in days, while the horizontal axis represents longitude. Positive (negative) lag values indicate the base point leads (lags). Contour interval is 0.1. Positive (negative) correlations are shown in red (blue) and the zero line is omitted.

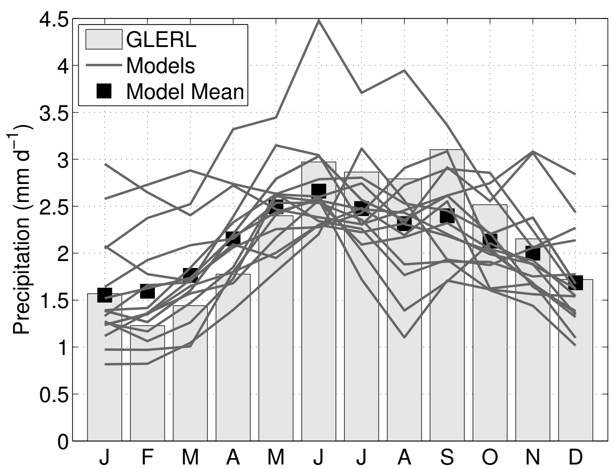


FIG. 6. Average monthly precipitation (mm day$^{-1}$) based on over-lake estimates from GLERL (grey bars) and each GCM used in the study (dark grey lines) between 1961-2000. Multi-model mean precipitation is shown as the black squares. Model precipitation is an average of precipitation from the grid cell closest to Lake Superior (48°N, 272°E) and the two adjacent cells at the same latitude.

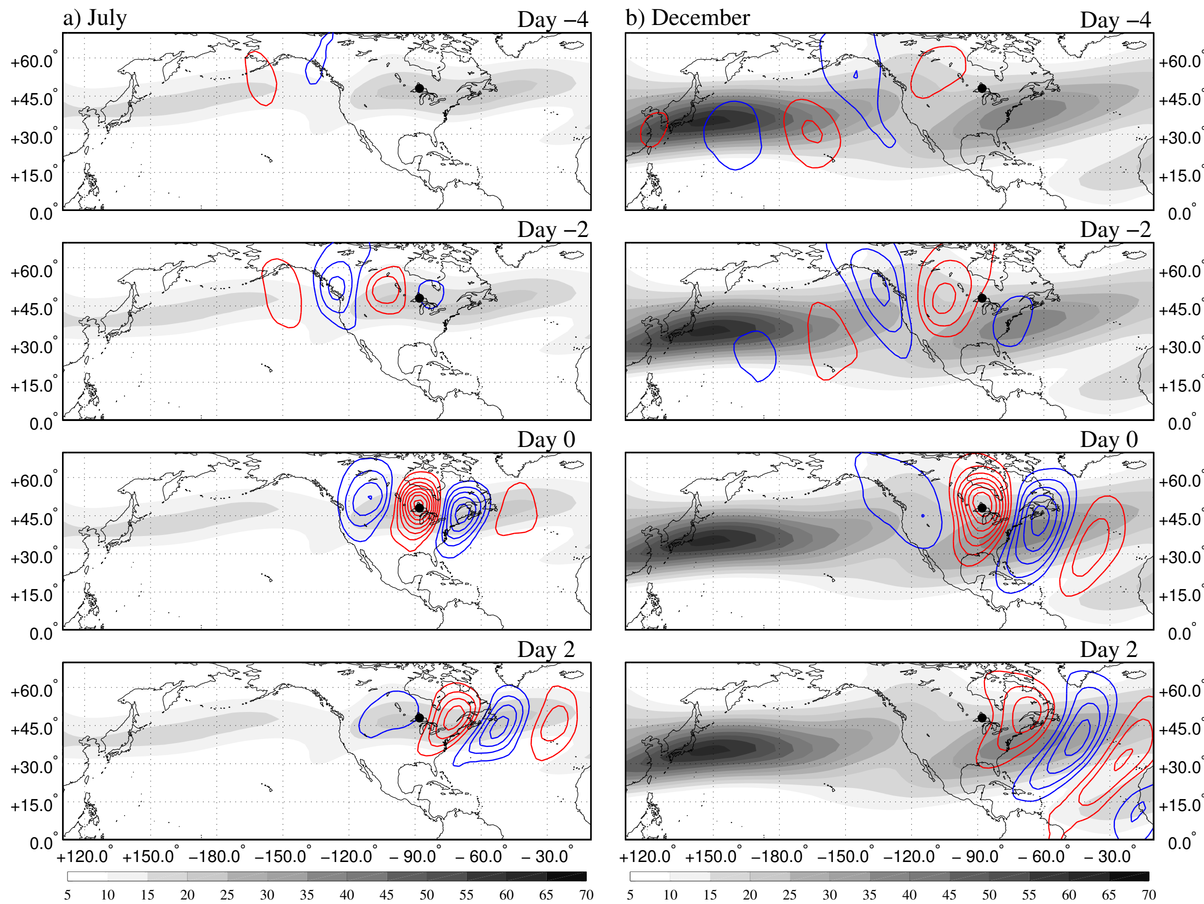


FIG. 7. Multi-model average time-lag correlation maps between daily 300 hPa meridional wind anomalies at each grid cell and a base point of daily precipitation anomalies averaged over three grid cells centered on Lake Superior (48°N, 272°E) during (a) July and (b) December. Negative (positive) lag values indicate the meridional wind anomalies precede (follow) the base point. The contour interval is 0.05. Positive (negative) correlations are shown in red (blue), and the zero line is omitted. Shading indicates the multi-model average monthly 300 hPa zonal wind speed (m $s^{-1}$) between 1961-2000.

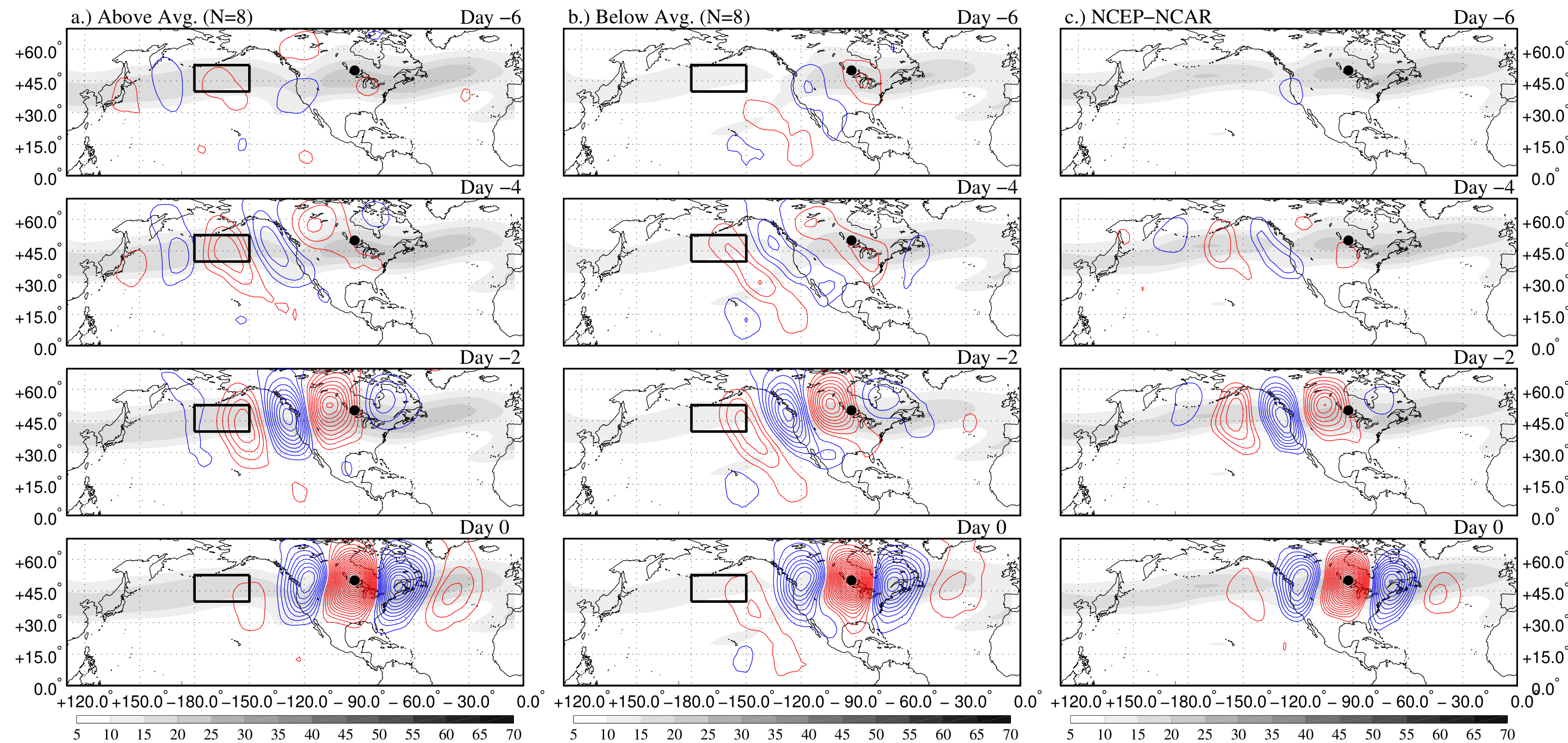


FIG. 8. Multi-model composite of July time-lag correlation maps (base point 50.0°N, 267.5°E; identified by the black dot) for models with (a) above- and (b) below- average 300 hPa zonal wind in the region outlined by the black box (40°-52.5°N and 180°-150°W) between 1961-2000. There are eight models in each pool. (c) Observed July time-lag correlation maps (contours) between daily 300 hPa meridional wind at 50.0°N, 267.5°E and 300 hPa meridional wind anomalies at every point between 1948-2010. The contour interval is 0.05 and positive (negative) correlations are shown in red (blue). Shading represents the average 300 hPa zonal wind (m $s^{-1}$) (a, b) among models and (c) from NCEP-NCAR reanalysis.

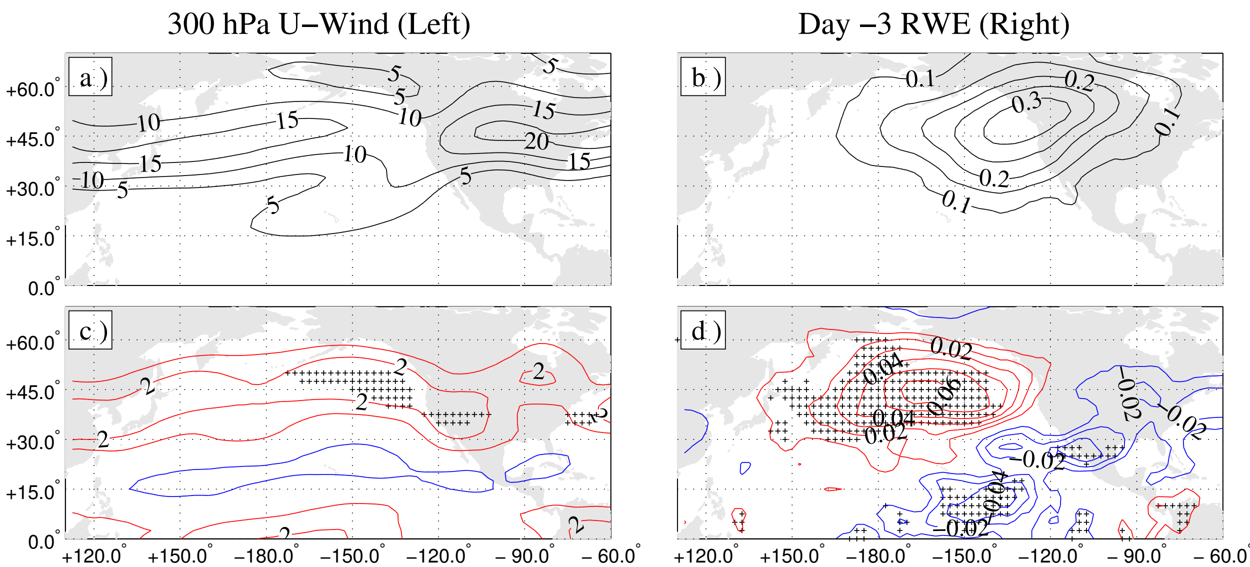


FIG. 9. July results from MCA of simulated 300 hPa zonal wind and day -3 RWEs. Multi-model average of mean July (a) 300 hPa zonal wind (m $s^{-1}$) and (b) Day -3 RWE of one-point correlation map between 1961-2000. (c) Heterogeneous map of 300 hPa zonal wind regressed onto day -3 RWE expansion coefficients. Red (blue) contours represent positive (negative) perturbation isotachs in units of 1 m $s^{-1}$, with the zero-line omitted. (d) Heterogeneous map of day -3 RWE patterns regressed onto 300 hPa zonal wind expansion coefficients. Red (blue) contours represent positive (negative) correlation perturbations in units of 0.01, with the zero-line omitted. Stippling indicates statistical significance based on the 95th percentile from 1000 Monte Carlo simulations at each grid cell.

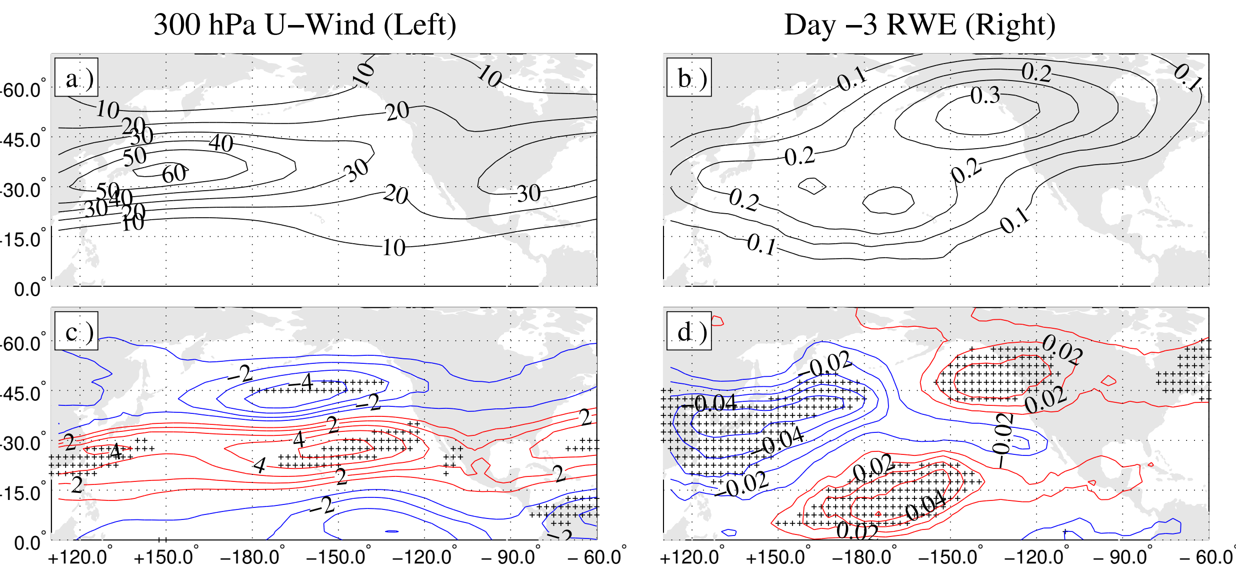


FIG. 10. Same as Fig. 9, except for December.

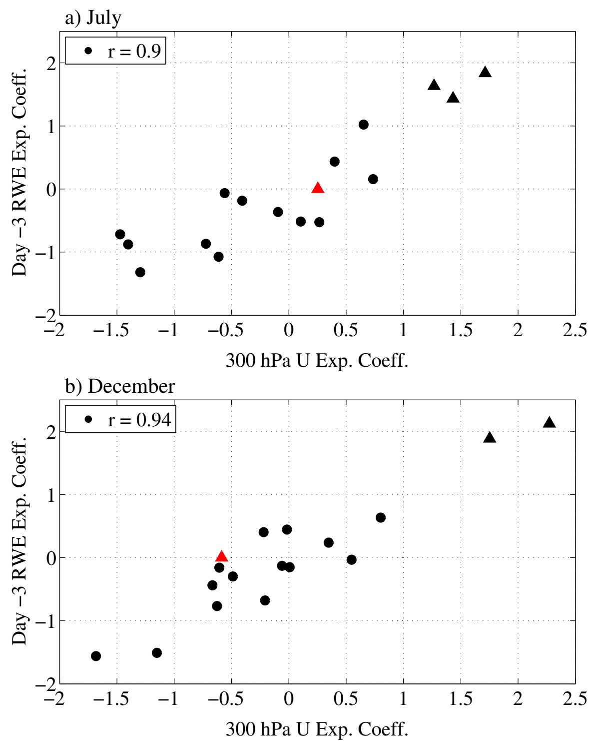


FIG. 11. Scatter plot showing day -3 RWE expansion coefficients versus 300 hPa zonal wind speed expansion coefficients based on the MCA analysis for each model (black circles and triangles) and NCEP-NCAR reanalysis (red triangle; see text for description) during (a) July and (b) December between 1961-2000. Correlations among model data are shown in the upper left of each plot.

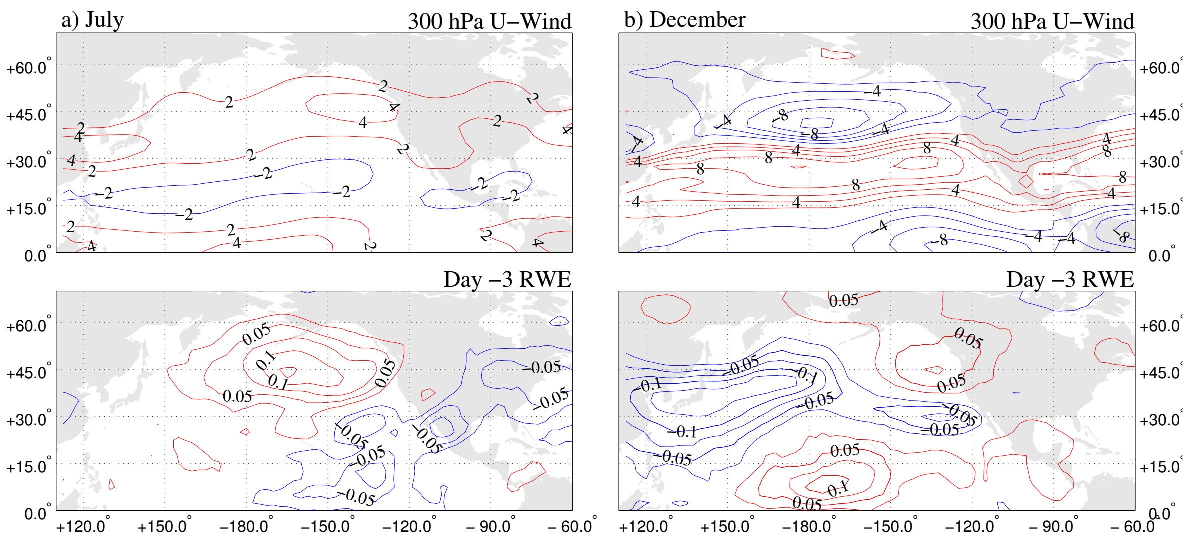


FIG. 12. Composites of simulated (top) 300 hPa zonal wind (m $s^{-1}$) and (bottom) Day -3 RWE anomalies (relative to the multi-model mean) during (a) July and (b) December based on outliers in Fig. 11a, b, respectively (see text for details). The contour interval in the top (bottom) plots is 2 m $s^{-1}$ (0.025). Zero lines are omitted.

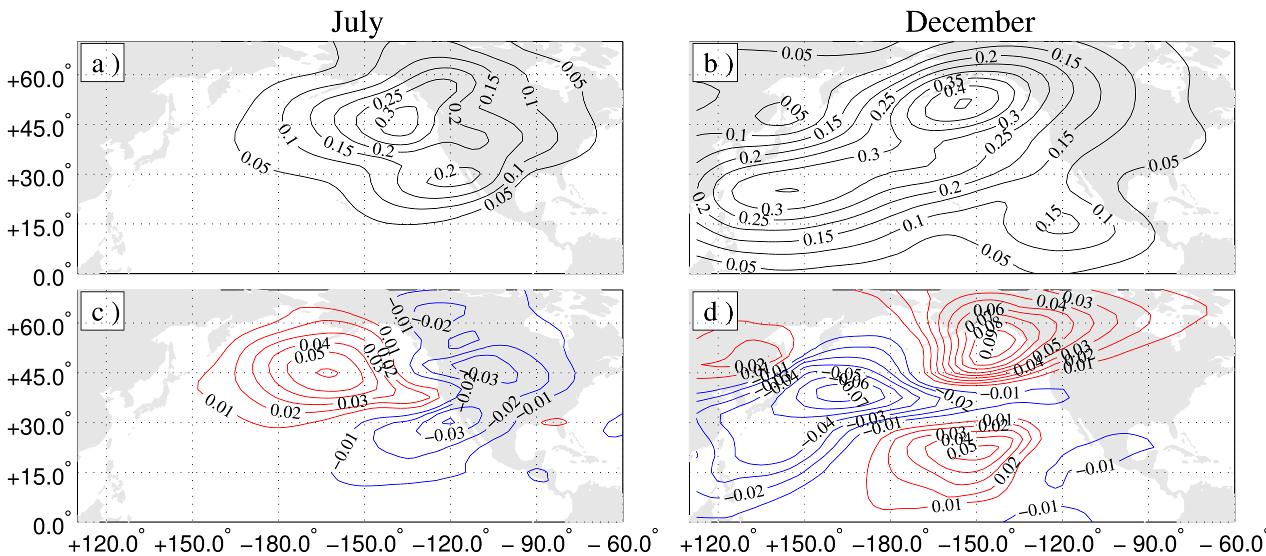


FIG. 13. (a) The RWE at day -3 from the barotropic model with a background state from the multi-model mean in July. (b) Same as (a) but for December. The contour interval is 0.05. (c) The July difference in RWE at day -3 from the barotropic model with background winds from the multi-model mean plus the MCA pattern and the barotropic model with background winds from the multi-model mean minus the MCA pattern. The pattern is divided by two to allow direct comparison with the MCA analysis. (d) Same as (c) but for December. Red (blue) contours represent positive (negative) values. The contour interval is 0.01, and the zero-line omitted.